

# Journal of Biomedical Optics

BiomedicalOptics.SPIEDigitalLibrary.org

## Cone-beam x-ray luminescence computed tomography based on x-ray absorption dosage

Tianshuai Liu  
Junyan Rong  
Peng Gao  
Wenli Zhang  
Wenlei Liu  
Yuanke Zhang  
Hongbing Lu

**SPIE.**

Tianshuai Liu, Junyan Rong, Peng Gao, Wenli Zhang, Wenlei Liu, Yuanke Zhang, Hongbing Lu, "Cone-beam x-ray luminescence computed tomography based on x-ray absorption dosage," *J. Biomed. Opt.* **23**(2), 026006 (2018), doi: 10.1117/1.JBO.23.2.026006.

# Cone-beam x-ray luminescence computed tomography based on x-ray absorption dosage

Tianshuai Liu,<sup>†</sup> Junyan Rong,<sup>†</sup> Peng Gao, Wenli Zhang, Wenlei Liu, Yuanke Zhang, and Hongbing Lu\*  
Fourth Military Medical University, Department of Biomedical Engineering, Xi'an, Shaanxi, China

**Abstract.** With the advances of x-ray excitable nanophosphors, x-ray luminescence computed tomography (XLCT) has become a promising hybrid imaging modality. In particular, a cone-beam XLCT (CB-XLCT) system has demonstrated its potential in *in vivo* imaging with the advantage of fast imaging speed over other XLCT systems. Currently, the imaging models of most XLCT systems assume that nanophosphors emit light based on the intensity distribution of x-ray within the object, not completely reflecting the nature of the x-ray excitation process. To improve the imaging quality of CB-XLCT, an imaging model that adopts an excitation model of nanophosphors based on x-ray absorption dosage is proposed in this study. To solve the ill-posed inverse problem, a reconstruction algorithm that combines the adaptive Tikhonov regularization method with the imaging model is implemented for CB-XLCT reconstruction. Numerical simulations and phantom experiments indicate that compared with the traditional forward model based on x-ray intensity, the proposed dose-based model could improve the image quality of CB-XLCT significantly in terms of target shape, localization accuracy, and image contrast. In addition, the proposed model behaves better in distinguishing closer targets, demonstrating its advantage in improving spatial resolution. © 2018 Society of Photo-Optical Instrumentation Engineers (SPIE) [DOI: 10.1117/1.JBO.23.2.026006]

Keywords: absorption dosage; imaging model; tomographic imaging; x-ray luminescence.

Paper 170666R received Oct. 12, 2017; accepted for publication Jan. 22, 2018; published online Feb. 22, 2018.

## 1 Introduction

With the advances of x-ray excitable nanophosphors, x-ray luminescence computed tomography (XLCT) has attracted more attention for its promising performance.<sup>1–3</sup> In XLCT, x-ray excitable nanophosphors are used as imaging probes and emit visible or near-infrared (NIR) light when irradiated by x-rays. By solving an inverse problem using an appropriate imaging model of x-ray and photon transport, the three-dimensional (3-D) distribution of the nanophosphors in the imaged object can be resolved. Compared with traditional bio-optical imaging modalities, such as bioluminescence tomography<sup>4,5</sup> and fluorescence molecular tomography,<sup>6,7</sup> XLCT can achieve higher sensitivity as well as higher spatial resolution due to the high penetrability/collimation of x-rays in biological tissues and the avoidance of autofluorescence during luminescent imaging.<sup>1–3</sup> As a hybrid x-ray CT/optical imaging modality, XLCT has become a promising imaging technique for fundamental research, drug development, and clinical studies.<sup>8–13</sup>

After the first demonstration of XLCT,<sup>1–3</sup> continuous studies have been devoted to improvements of its imaging performance and various XLCT imaging systems have been proposed.<sup>14–22</sup> Among them, a narrow-beam XLCT system could provide the highest spatial resolution; however, the imaging time seems incredibly long due to the complicated data acquisition mode.<sup>14–16</sup> To reduce the scan time, a cone-beam XLCT (CB-XLCT) imaging system was recently implemented by Chen et al.<sup>17–19</sup> and then applied to small animal imaging by Liu et al.<sup>20</sup> Compared with the narrow-beam XLCT, CB-XLCT could speed up imaging significantly at the cost of

spatial resolution.<sup>21</sup> To improve the reconstruction quality of CB-XLCT, Liu et al.<sup>20,21</sup> combined a compressive sensing (CS) technique with wavelet transform to improve tomographic images reconstructed from single-view data. Zhang et al.<sup>22</sup> further proposed a self-adaptive Bayesian method for CB-XLCT reconstruction and validated its superiority with numerical simulations and mouse experiments.

Currently, the imaging model of most XLCT systems is based on the assumption that nanophosphors emit light based on the intensity distribution of x-rays within the object,<sup>16–22</sup> which can be estimated by the Lambert–Beer law. Considering the complicated energy transfer from x-ray photons to electrons and luminescence centers of phosphors, the assumption may not reflect the nature of the x-ray excitation process accurately.<sup>3</sup> Previous studies have indicated that optical luminescence of nanophosphors excited by x-rays depends more on x-ray dosage, instead of x-ray intensity.<sup>23–25</sup> Based on the assumption that optical source intensity was proportional to the x-ray dosage and the concentration of phosphors, Li et al.<sup>15</sup> proposed a reconstruction algorithm for the narrow-beam XLCT in which the position of narrow-beam x-rays was used as excitation priors, and they validated the algorithm with numerical simulations. This suggests that a forward model based on x-ray absorption dosage may better reflect the energy-related excitation process of nanophosphors. However, for cone-beam XLCT imaging, all nanophosphors in a 3-D region can be excited simultaneously when irradiated by x-rays. The excitation priors used in the narrow-beam XLCT reconstruction were not valid any more.

In this paper, we first propose a forward model based on x-ray absorption dosage for CB-XLCT imaging. Based on

\*Address all correspondence to: Hongbing Lu, E-mail: [luhb@fmmu.edu.cn](mailto:luhb@fmmu.edu.cn)

<sup>†</sup>These authors contributed equally to this work and are the cofirst authors for this paper.

the x-ray absorption dose distribution estimated from the attenuation map of the imaged object by the widely used GATE package,<sup>26,27</sup> a reconstruction algorithm that combines the adaptive Tikhonov regularization method (ADAPTIK) with the imaging model is implemented. To validate the proposed model and algorithm, numerical simulations and phantom experiments are performed and CB-XLCT images reconstructed using different models are evaluated quantitatively.

## 2 Theory

### 2.1 Forward Model of X-Ray Luminescence Computed Tomography

In XLCT imaging, x-rays emitted by the x-ray source travel through the biological tissues and provide an excitation field inside the imaging object. Currently, the excitation field of most XLCT systems is derived from the intensity distribution of the x-rays within the object, which can be given by the Lambert-Beer law<sup>20,21</sup>

$$X(r) = X(r_0) \exp \left[ - \int_{r_0}^r \mu(\tau) d\tau \right], \quad (1)$$

where  $X(r_0)$  is the intensity of x-rays at the initial position of  $r_0$ , and  $\mu(\tau)$  represents the x-ray attenuation coefficient at position  $\tau$ .

For XLCT imaging, when irradiated by x-rays, nanophosphors inside the object can emit visible or NIR light. Based on previous studies,<sup>21,22</sup> the number of optical photons emitted by nanophosphors can be expressed as

$$S(r) = \varepsilon X(r) n(r), \quad (2)$$

where  $S(r)$  is the light emitted [ $\text{W}/\text{cm}^3$ ],  $n(r)$  is the concentration of nanophosphors [ $\text{mg}/\text{ml}$ ],  $\varepsilon$  is the light yield [ $\text{cm}^3/\text{mg}$ ], and  $X(r)$  is the intensity of x-rays at position  $r$  [ $\text{W}/\text{cm}^3$ ].

As we know, x-ray luminescence (XL) has been well characterized for bulk inorganic scintillators.<sup>23</sup> Briefly, the scintillator can be defined as a wavelength shifter. It converts an x-ray photon of high energy into a number of photons of much lower energy in the visible or near visible range, which can be easily detected with sensitive photo detectors, such as an electron-multiplying charge-coupled device (EMCCD) camera. Based on a previous study,<sup>22</sup> the light yield  $Y$  of the scintillation can be given by the following formulation:

$$Y = \frac{E_\gamma}{E_g} \cdot T \cdot Q, \quad (3)$$

where  $E_\gamma$  is the absorbed energy,  $E_g$  is the mean energy necessary for the formation of one thermalized electron,  $T$  is the efficiency of the energy transfer from thermalized pairs to the excited states of luminescent centers, and  $Q$  is the quantum yield of the intracenter luminescence.

The above x-ray luminescence theory suggests that the excitation field of nanophosphors depends more on the absorbed energy, which could be reflected by x-ray absorbed dose, including those induced by scattering x-rays. By assuming the number of optical photons emitted, which is proportional to the absorbed dosage of the x-rays and the concentration of nanophosphors in the object, we propose a dosage-based excitation model as below

$$S(r) = \Gamma X_d(r) n(r). \quad (4)$$

Here,  $S(r)$  and  $n(r)$  are the same as those defined in Eq. (2).  $\Gamma$  is defined as an energy-emission efficiency parameter with the unit of  $\text{W}/(\text{Gy}\cdot\text{mg})$ , and  $X_d(r)$  represents absorbed x-ray dose at position  $r$  [ $\text{Gy}$ ].

Considering the high scattering and low absorption of the visible and NIR light in biological tissues, the propagation model of the emitted light in biological tissues can then be established by the diffusion equation (DE)<sup>22</sup>

$$-\nabla \cdot [D(r)\nabla\Phi(r)] + \mu_a(r)\Phi(r) = S(r) \quad (r \in \Omega), \quad (5)$$

where  $\Omega$  is the image domain,  $\Phi(r)$  is the photon fluence, and  $\mu_a(r)$  is a absorption coefficient.  $D(r)$  represents a diffusion coefficient that can be calculated by  $D(r) = 1/[3(\mu'_s(r) + \mu_a(r))]$  in which  $\mu'_s(r)$  is a reduced scattering coefficient.

To solve the diffusion Eq. (5), Robin boundary conditions are usually applied as below:<sup>28,29</sup>

$$\Phi(r) + 2\kappa D(r)[\nu\nabla\Phi(r)] = 0 \quad (r \in \partial\Omega), \quad (6)$$

where  $\partial\Omega$  represents the boundary of  $\Omega$ ,  $\kappa$  is a boundary mismatch parameter, and  $\nu$  represents the outward unit normal vector on the boundary. This assumes that for a nonscattering medium surrounding  $\Omega$ , no diffuse surface reflection at  $\partial\Omega$  occurs.

With the finite-element method (FEM), Eqs. (5) and (6) can be discretized into a matrix equation as

$$A\Phi = \Gamma F N, \quad (7)$$

with

$$a_{ij} = \int_{\Omega} [D(r)\nabla\psi_i(r)\nabla\psi_j(r) + \mu_a(r)\psi_i(r)\psi_j(r)] dr + \frac{1}{2\kappa} \int_{\partial\Omega} D(r)\psi_i(r)\psi_j(r) dr, \quad (8)$$

$$f_{ij} = \int_{\Omega} X_d(r)\psi_i(r)\psi_j(r) dr, \quad (9)$$

where  $N$  is the distribution vector of nanophosphors and  $a_{ij}$  and  $f_{ij}$  are the elements of matrix  $A$  and  $F$ , respectively.  $\psi_i(r)$  and  $\psi_j(r)$  are the corresponding elements of discretized geometrical meshes of the imaging domain, and  $X_d(r)$  is the x-ray dose absorbed at position  $r$ .

Since the matrix  $A$  is positive definite, Eq. (7) can be further recast into

$$\Phi = MN, \quad (10)$$

where  $M = \Gamma A^{-1} F$  and  $\Phi$  represents the distribution vector of photon fluence. For optical tomography, only intensity values of  $\Phi$  on the object surface could be measured; then, Eq. (10) becomes

$$\Phi_{\text{meas}} = WN, \quad (11)$$

where  $\Phi_{\text{meas}}$  is the vector of photon fluence acquired on the object surface and  $W$  consists of rows of the weight matrix  $M$  corresponding to surface measurements.  $W$  describes the forward model of the XLCT imaging and was acquired by

the COMSOL Multiphysics 3.3 (COMSOL, Inc., Burlington, Massachusetts) in this study. During phantom simulations and experiments, the geometric model of each phantom was first established, and then the imaging domain was discretized into finite-element meshes. For the intensity-based forward model, the intensity distribution of x-ray calculated by the Lambert–Beer law was input as the excitation field. For the dose-based forward model, the dose distribution of x-ray was estimated by Monte Carlo simulation package GATE and then input as the excitation field.

## 2.2 Image Reconstruction of Cone-Beam X-Ray Luminescence Computed Tomography

The goal of the XLCT reconstruction is to estimate the nanophosphor distribution  $N$  from  $\Phi_{\text{meas}}$ . Cone-beam XLCT reconstruction is a severe ill-posed problem in which the solution is usually underdetermined and noise-sensitive. To alleviate the problem, the ADAPTIK is adopted in this study.<sup>30</sup>

The solution to Eq. (11) with the ADAPTIK method is given by

$$N = [W^T W + \text{tr}(W^T W)\Lambda]^{-1} W^T \Phi_{\text{meas}}, \quad (12)$$

where  $\text{tr}()$  denotes the trace of a matrix, and  $\Lambda$  is a diagonal matrix composed of spatially varying regularization parameters as

$$\Lambda = \begin{Bmatrix} \alpha_i(1) & \cdots & 0 \\ \vdots & \ddots & \vdots \\ 0 & \cdots & \alpha_i(r) \end{Bmatrix}. \quad (13)$$

Each element  $\alpha_i(r)$  of  $\Lambda$  is a spatially varying regularization parameter that is adaptively updated based on the results of the previous iteration.

The principle of the ADAPTIK method is to spatially penalize different voxels of the reconstructed image using adaptively updated regularization parameters. With the spatially varying regularization, the region with fluorescent probe could be preserved and the background would be smoothed. In the process of reconstruction, a threshold  $\alpha_{\text{stop}}$  is used to avoid unstable solutions caused by too small regularization parameters  $\alpha_i(r)$ . Please refer to Ref. 30 for a detailed description of the ADAPTIK method and parameter settings.

## 3 Experimental Design

Numerical simulations and phantom experiments were performed to evaluate the performance of the proposed forward model on CB-XLCT reconstructions. As an essential step before reconstruction, the x-ray dose distribution within the imaged object was first estimated by GATE. Then all XLCT images were reconstructed by the ADAPTIK algorithm. For comparison, the traditional forward model based on the x-ray intensity was also used. Considering the tradeoff between imaging quality and reconstruction time, in this study, the stopping criterion  $\alpha_{\text{stop}}$  was set as  $10^{-8}$  and the number of iterations was set as 8 for all numerical simulations and phantom experiments, as suggested in Ref. 30.

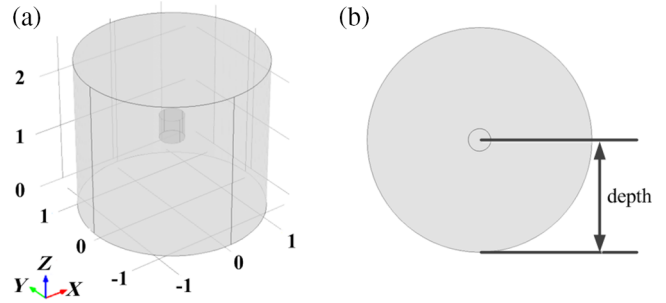


**Fig. 1** The cylinder phantom used in simulation studies. (a) A 3-D view of the phantom and (b) the overhead view of the phantom. The depth is defined as the distance from the target center to the outer surface of the cylinder.

## 3.1 Numerical Simulations

Numerical simulations using two different phantoms were performed to validate the proposed CB-XLCT excitation model based on x-ray absorbed dosage. One was a simple phantom with a target positioned at different depths in a cylinder tank, which was used to evaluate the effect of target position on the proposed model. Another employed a complicated Digimouse phantom to make the simulations more realistic.

### 3.1.1 Simulations with a cylinder phantom

The cylinder phantom was composed of a large cylinder tank (3.0 cm in diameter and 2.3 cm in height) and a small tube (4 mm in diameter and 4 mm in height) filled with  $\text{Y}_2\text{O}_3:\text{Eu}^{3+}$ , which was placed inside the cylinder as a target, as shown in Fig. 1. The tank was filled with a mixture of water and Intralipid and the optical properties were set as  $\mu_a = 0.03 \text{ cm}^{-1}$  and  $\mu'_s = 10 \text{ cm}^{-1}$ . In this study, the optical properties of the tank phantom were obtained from Refs. 21 and 31 not measured from x-ray excitation.

To evaluate the influence of target position on the proposed model, numerical simulations were performed with the target tube in Fig. 1 positioned at different depths of 15, 11, and 7 mm (the distance between the tube center and the outer surface of the cylinder).

### 3.1.2 Simulation with a Digimouse

To test the performance of the proposed model with a more realistic phantom, a Digimouse phantom was implemented and used for simulations. As shown in Fig. 2(a), the 3-D Digimouse model consists of different parts including the heart, liver, spleen, lung, bone, and stomach.<sup>6,7</sup> Two cylindrical tubes (4 mm in diameter and 4 mm in height) filled with  $\text{Y}_2\text{O}_3:\text{Eu}^{3+}$  (density: 7.4 g/ml) were placed in the liver as targets. Figure 2(b) shows the 3-D locations of the two targets, and Fig. 2(c) shows a representative slice across the targets. The edge-to-edge distance between the two targets was 6 mm. A heterogeneous digital model was constructed by assigning adequate optical properties to the segmented organs. Please refer to Ref. 7 for a detailed description on the model and related parameters.

### 3.1.3 Simulation settings

For phantom simulations, the imaging model is discretized into 2695 nodes and 12,285 tetrahedral elements in a 3-D region

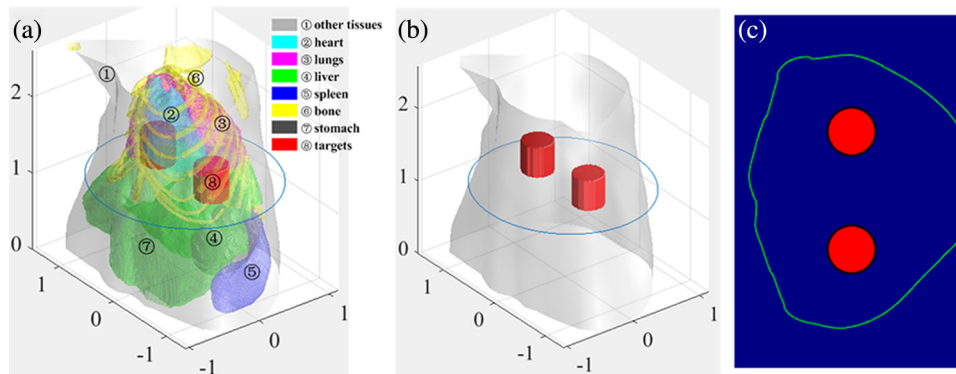


**Fig. 2** (a) The 3-D Digimouse model used for simulation studies, (b) a 3-D locations of the two targets, and (c) a slice of the simulation model corresponding to the blue line in (a).

of  $3.0 \times 3.0 \times 2.3 \text{ cm}^3$ , and, for the Digimouse simulation, the imaging model is discretized into 6827 nodes and 32,610 tetrahedral elements in a 3-D region of  $2.0 \times 3.0 \times 2.5 \text{ cm}^3$ .

To make the results comparable with phantom experiments, in all numerical simulations, the distance from the x-ray source to the rotation center of the imaging system was set as 26.3 cm, and the EMCCD camera was positioned perpendicularly to the x-ray source-detector axis, with a distance of 45 cm between the CCD center and the rotation center. The voltage and current of the cone beam x-ray source were set as 50 kVp and 0.5 mA, respectively. The simulated projection was obtained every 15 deg during a 360-deg scan.

After optical luminescence was obtained at different angles, white Gaussian noise was added into all projections with a zero-mean and signal-to-noise ratio of 30 DB to simulate noisy measurements.<sup>22</sup> Then the ADAPTIK method was used to reconstruct nanoparticle distribution inside the phantom, with the proposed x-ray dosage model and the x-ray intensity model, respectively.

### 3.2 Phantom Experiments

To further validate the proposed dose-based model and reconstruction method with real luminescence measurements, a series of phantom experiments were performed using a custom-developed CB-XLCT system, based on observations from simulation studies.

#### 3.2.1 Cone-beam x-ray luminescence computed tomography imaging system

Figure 3 gives a schematic diagram of the CB-XLCT system used in this study. The system includes a microfocus x-ray source (SB-80-500, New York), a rotation stage, an EMCCD camera (iXon DU-897, Andor, United Kingdom) for optical imaging, and a flat-panel x-ray detector (2923, Dexela, United Kingdom) for high-resolution CT imaging. The maximum voltage of the x-ray source is 80 kVp with the maximum power of 80 W, and the distance from the x-ray source to the rotation center of the imaging system was 26.3 cm. The EMCCD camera coupled with a Nikon 50-mm  $f/1.8D$  lens was positioned at 90 deg toward the x-ray source-detector axis, with a distance of 45 cm to the rotation center. The minimum cooling temperature of the EMCCD camera is  $-80 \text{ deg}$ , which can effectively reduce the dark noise. During the luminescence imaging, the system was enclosed in a light-tight environment to avoid outside light.

#### 3.2.2 Phantom configuration

The configuration of the physical phantom used in imaging experiments is shown in Fig. 4. A glass cylinder (3.0 cm in diameter, 4.0 cm in height) containing a mixture of water and Intralipid was fixed on the rotation stage. Two small glass tubes (3 mm in diameter) filled with  $\text{Y}_2\text{O}_3:\text{Eu}^{3+}$  of a density of 7.4 g/ml were symmetrically placed in the cylinder to simulate

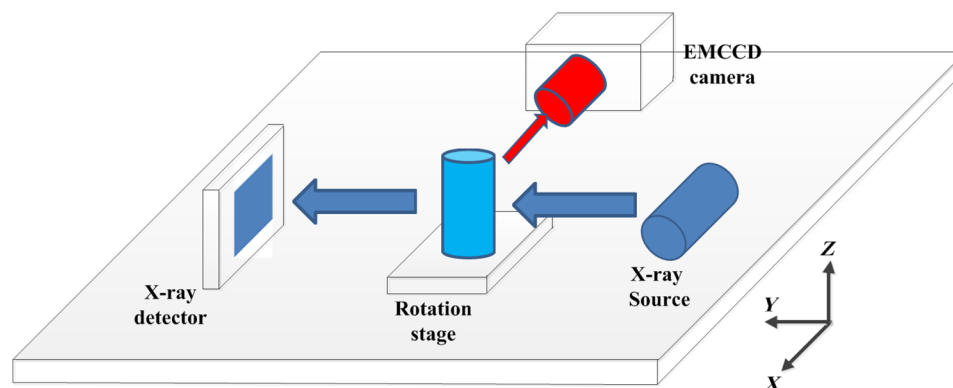


**Fig. 3** The schematic diagram of the CB-XLCT system.

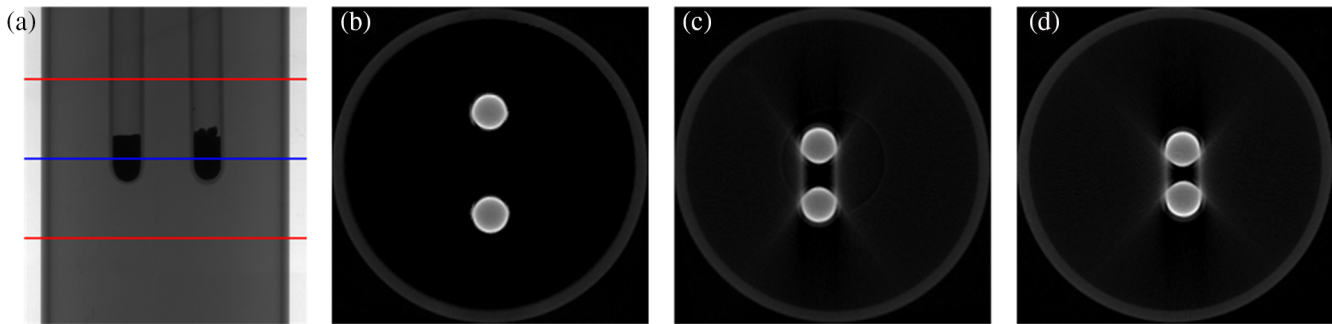


**Fig. 4** The physical phantom used in imaging experiments. (a) An x-ray projection of the phantom. The region between two red lines is used for reconstruction in this study. (b)–(d) CT slices of the phantom, corresponding to the position indicated by the blue line in (a), with different edge-to-edge distance between the two targets, (b) 6.3 mm, (c) 2.5 mm, and (d) 1.5 mm, respectively.

two targets. The edge-to-edge distance between the two tubes was 6.3 mm, as shown in Figs. 4(a)–4(b).

To further evaluate the performance of the proposed method on spatial resolution, two additional phantom experiments were performed, by setting the edge-to-edge distance between the two targets as 2.5 and 1.5 mm, respectively, as shown in Figs. 4(c)–4(d).

During imaging experiments, the voltage and current of the x-ray source were set as 50 kVp and 0.5 mA, respectively. The phantom was rotated from 0 deg to 360 deg and the optical images were obtained every 15 deg by the EMCCD camera. The exposure time of the EMCCD camera was set as 1 s.

### 3.2.3 X-ray CT reconstruction

After XLCT imaging, the structural information of the phantoms was also acquired with the developed system, such as a conventional micro-CT (X-CT). The flat-panel detector was positioned at a distance of 62 cm to the rotation center, and the projections were acquired with an angular increment of 1 deg. The voltage and current of the x-ray source were set as 50 kVp and 0.5 mA, respectively, and the acquisition time for each projection was 600 ms. The Feldkamp–Davis–Kress (FDK) algorithm was used for CT reconstruction.<sup>32,33</sup> With the attenuation maps obtained by x-CT, experimental conditions were simulated with GATE to estimate x-ray dose distribution for digital and phantom experiments.

### 3.3 X-Ray Dose Estimation Using GATE

In our study, the forward model of XLCT is established based on the dose distribution of x-rays within the imaged object. For the light excitation and acquisition process at each projection of CB-XLCT imaging, the x-ray dose distribution was estimated by GATE V7.1, with the consideration of x-ray scattering and absorbing in the object. Since x-ray scattering can be incoherent (Compton scattering) or coherent (Rayleigh scattering), both types of scattering were included during the estimation.

For accurate estimation of x-ray dose distribution, the polyenergetic property of x-rays for different tube voltages was considered by the simulation package available on the website<sup>34</sup> based on the known tungsten anode of the x-ray tube, as shown in Fig. 5. In our experiments, the energy spectrum of 50 kVp was used in GATE for dose estimation.

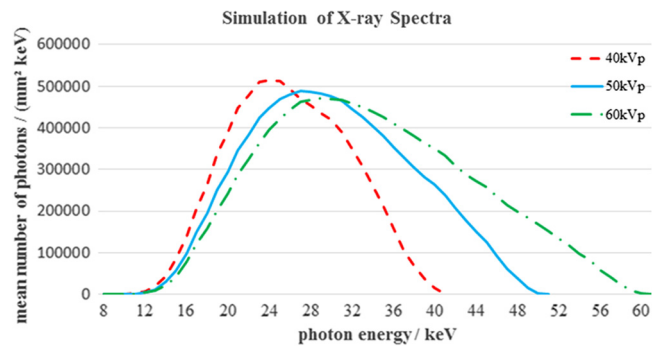


**Fig. 5** X-ray photon energy spectra used in GATE simulations (the red line: x-ray spectrum of 40 kVp, blue line: 50 kVp, and green line: 60 kVp).

### 3.4 Quantitative Evaluation of X-Ray Luminescence Computed Tomography Projections and Reconstructed Images

To evaluate the accuracy of the proposed forward model, the normalized mean square error (NMSE) of the measured and predicted projections was calculated as below

$$\text{NMSE} = \frac{\|y_1 - y_2\|_2^2}{\|y_1\|_2^2}, \quad (14)$$

where  $y_1$  and  $y_2$  denote the EMCCD measurements and the projection predicted by the forward model at a fixed view, respectively.

The quality of reconstructed CB-XLCT images was evaluated quantitatively by several indexes including the location error (LE), dice similarity coefficient (DICE), and contrast-to-noise ratio (CNR).<sup>35</sup>

LE evaluates the localization accuracy of the reconstructed target, which is defined as the Euclidean distance error between the centers of true and reconstructed targets

$$\text{LE} = \|L_r - L_t\|_2, \quad (15)$$

where  $L_r$  and  $L_t$  denote the centers of the reconstructed and true targets, respectively.

DICE reflects the similarity of the true and reconstructed targets and can be calculated by

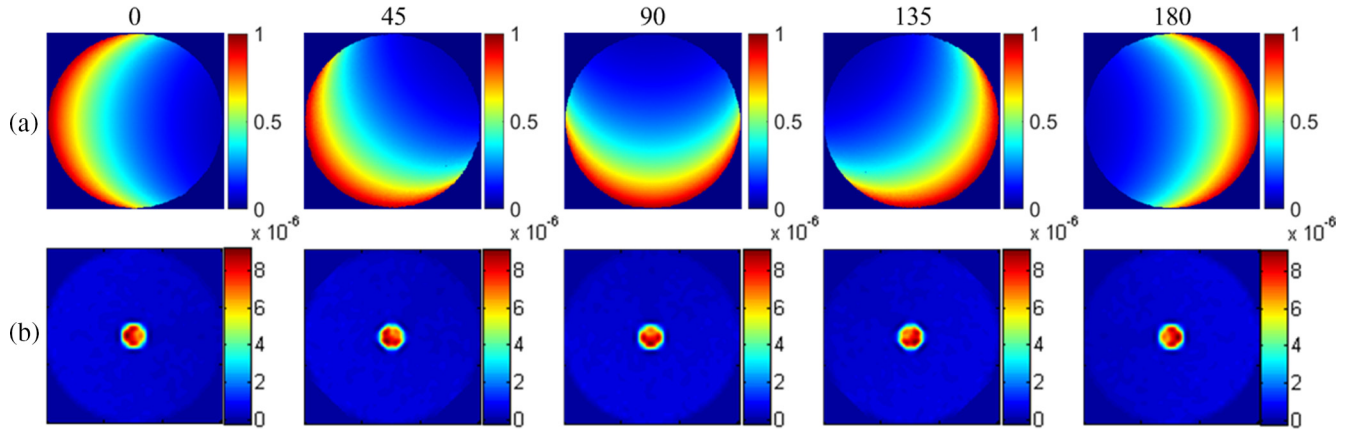


**Fig. 6** X-ray intensity and dose distributions for different projection views. (a) X-ray intensity distribution in the object and (b) x-ray dose maps with targets positioned at depths of 15 mm.

$$\text{DICE} = \frac{2|\text{ROI}_t \cap \text{ROI}_r|}{|\text{ROI}_t| + |\text{ROI}_r|}, \quad (16)$$

where  $\text{ROI}_t$  and  $\text{ROI}_r$  denote the regions of true and reconstructed targets, respectively, and  $|\cdot|$  defines the number of voxels in a region.

CNR is used for quantitative evaluation of noise and artifacts in reconstructed images, as shown below:

$$\text{CNR} = \frac{|\mu_{\text{ROI}} - \mu_{\text{BCK}}|}{(w_{\text{ROI}}\sigma_{\text{ROI}}^2 + w_{\text{BCK}}\sigma_{\text{BCK}}^2)^{1/2}}, \quad (17)$$

where ROI and BCK denote the target and background regions of the imaged object, respectively,  $w_{\text{ROI}}$  and  $w_{\text{BCK}}$  are the weighting factors determined by the relative volumes of the target and background, respectively,  $\mu_{\text{ROI}}$  and  $\mu_{\text{BCK}}$  are the mean intensity values of the ROI and BCK, respectively, and  $\sigma_{\text{ROI}}^2$  and  $\sigma_{\text{BCK}}^2$  represent the variances of the ROI and BCK, respectively.

## 4 Results

### 4.1 Comparison of Different Forward Models

In GATE simulations, the total number of x-ray photons in each projection was set to  $10^8$ . The distributions of the x-rays

intensity and x-ray dosage within the imaged object are shown in Fig. 6, with the target positioned at a depth of 15 mm. Please note that the x-ray intensity distribution was estimated by the Lambert–Beer law based on uniform assumption. From five representative projection views, it can be observed that x-ray intensity decreased along the traveling path. However, due to high attenuation of nanophosphors, high absorption dose regions could be found in areas where nanophosphors were located. In contrast, the dose in other regions was relatively low. This indicates that, compared with x-ray intensity, the dose distribution better reflects x-ray energy absorbed in the imaged object.

Theoretical analysis given in Sec. 2.1 indicates that the major difference between the intensity-based model and the proposed dose-based model is in the calculation of  $S(r)$ . For the nanophosphors used in this study,  $\Gamma$  and  $\epsilon$  were usually set as constants.<sup>3,22</sup> The difference between two forward models was, therefore, caused by the difference between  $X_d(r)$  and  $X(r)$ .

To evaluate the forward models, projections generated with different forward models were compared with CCD measurements acquired in the phantom experiment shown in Fig. 4(a). X-ray intensity distribution or dose map at each angle was estimated and used as the excitation field, as shown in Fig. 7, to generate a predicted projection. Figures 8(a)–8(c) give five representative views of CCD measurements and projections

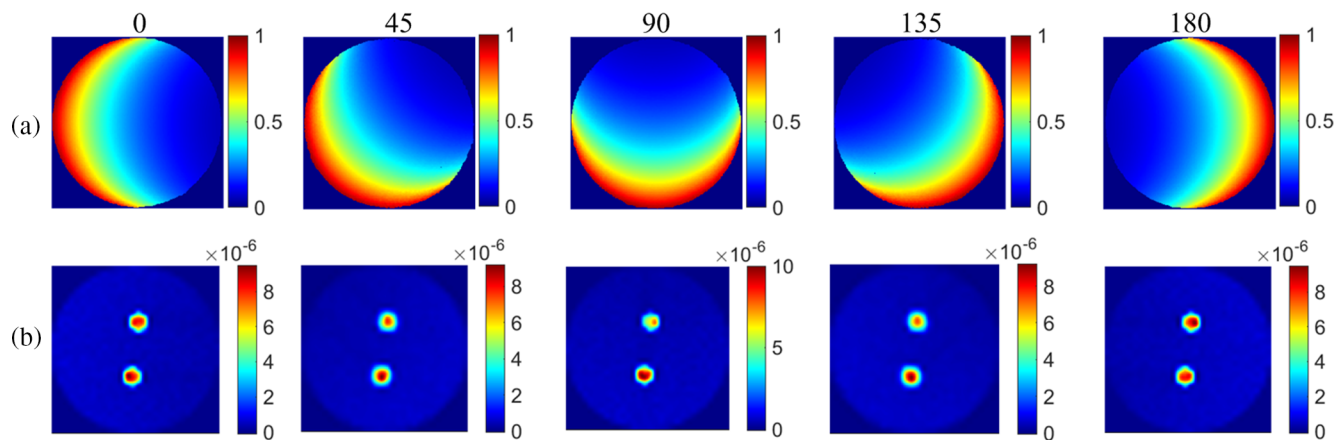


**Fig. 7** X-ray intensity and dose distributions of the experimental phantom for different projection views. (a) X-ray intensity distributions within the object and (b) x-ray dose distributions within the object.

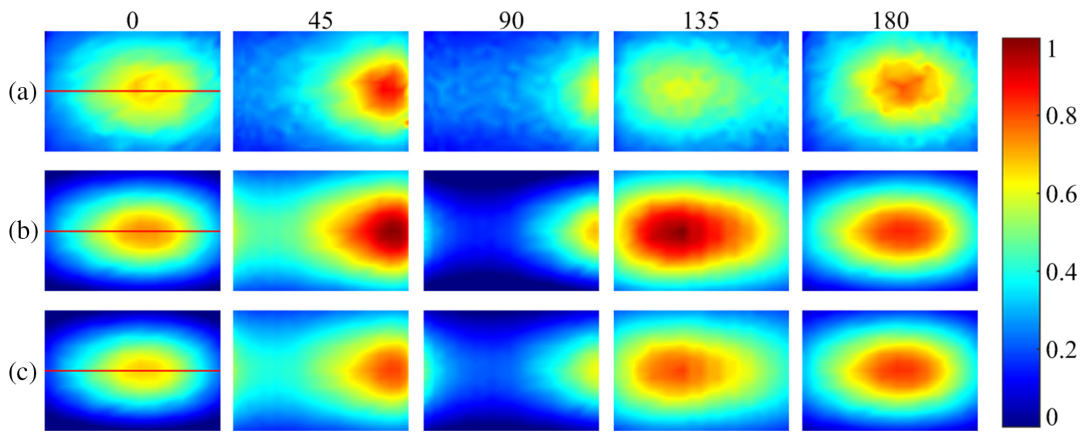


**Fig. 8** Representative luminescence projections acquired at five different angles (0 deg, 45 deg, 90 deg, 135 deg, and 180 deg). (a) Measured by the EMCCD camera in the phantom experiment, (b) prediction generated by the intensity-based model, and (c) prediction generated by the dose-based model.

predicted with different forward models. The corresponding luminescence profiles along the red lines shown in Fig. 8 are given in Fig. 9. It indicates that, compared with the intensity-based model, projections generated by the dose-based forward model agree better with CCD measurements in all given angles.

Table 1 summarizes the NMSE between the measurements and model predictions for five representative views and average NMSE values of all 24 luminescence projections. The quantitative results are consistent with visual observations from Figs. 8 and 9. It further confirms that the forward model

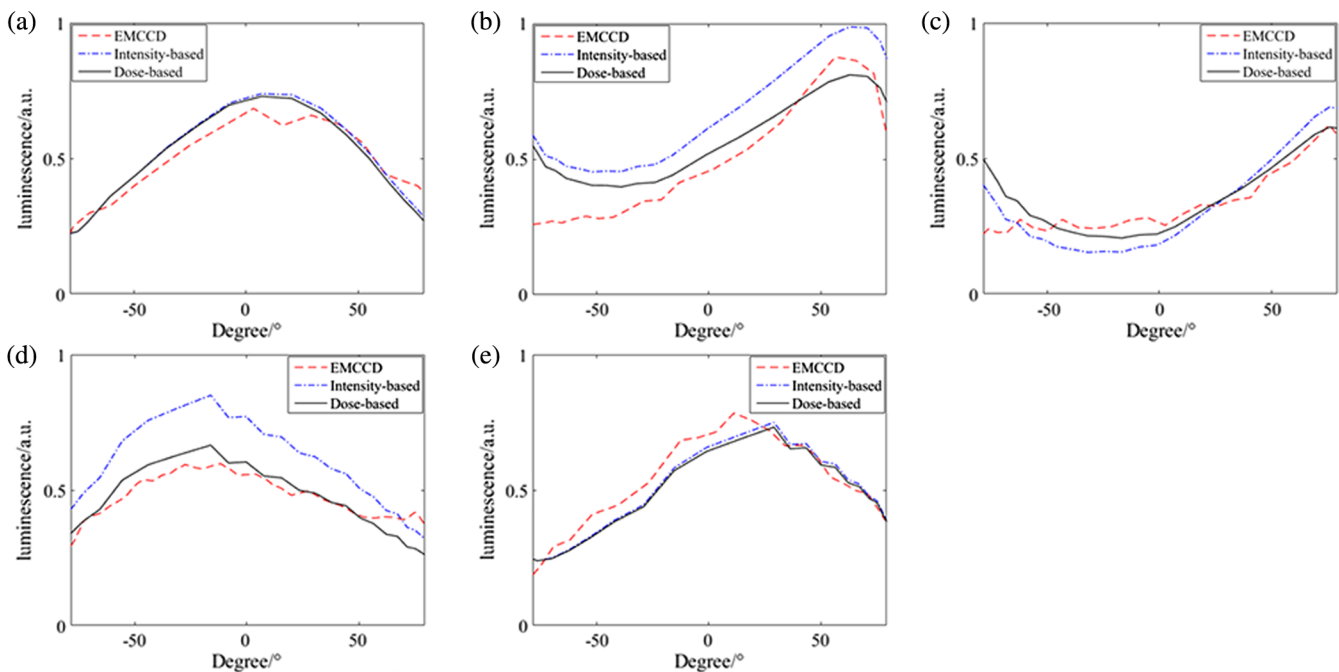


**Fig. 9** Luminescence profiles along the red line shown in Fig. 8 for the five representative excitation angles (a) 0 deg, (b) 45 deg, (c) 90 deg, (d) 135 deg, and (e) 180 deg. a.u., arbitrary unit.

**Table 1** Quantitative evaluation of the forward model.

Index	Forward model	0 deg	45 deg	90 deg	135 deg	180 deg	All angles
NMSE	X-ray intensity-based model	0.19	0.18	0.23	0.16	0.15	0.21
	X-ray dosage-based model	0.15	0.07	0.16	0.06	0.08	0.13

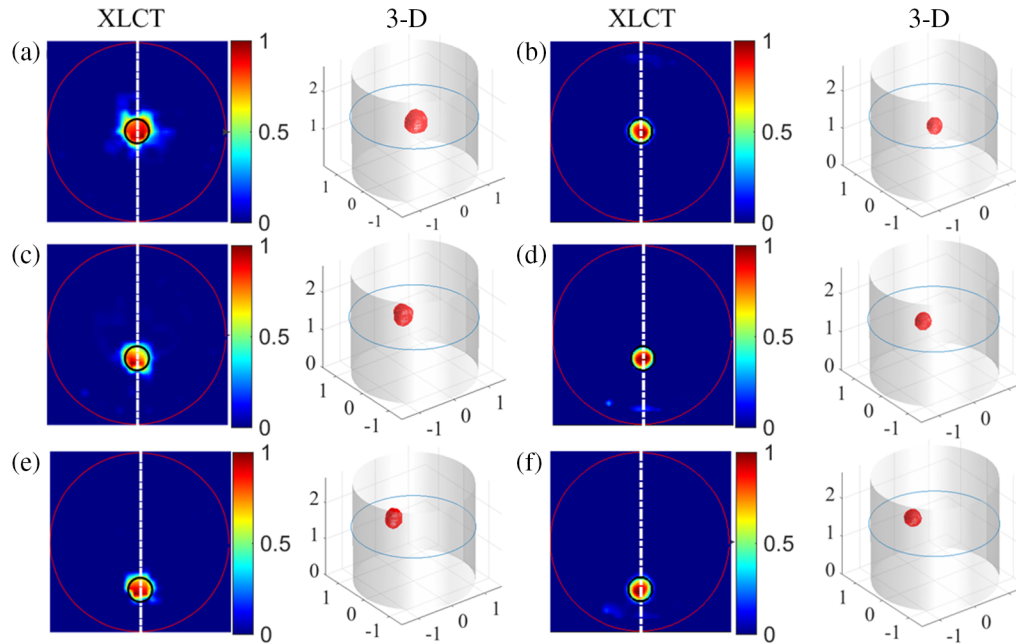


**Fig. 10** CB-XLCT reconstructions of targets positioned at different depths, (a)–(e) using the intensity-based model and (b)–(f) the dose-based model. From top to bottom: the target positioned at depth of 15, 11, and 7 mm, respectively.

based on x-ray absorbed dosage agrees better with the measurements acquired by phantom experiments.

#### 4.2 Numerical Simulations with Targets Positioned at Different Depths

The XLCT tomographic images of the targets positioned at three different depths were reconstructed using different forward models, as shown in Fig. 10. It clearly indicates that compared with the intensity-based model, the proposed model yielded consistent and better reconstructions in terms of target shape and localization accuracy at all tested depths.

**Table 2** Quantitative evaluation of reconstructed images for targets positioned at different depths.

Target depth/mm	Indexes	X-ray intensity-based model	X-ray dosage-based model
15	LE (mm)	0.5	0.14
	Dice	0.56	0.95
	CNR	10.2	18
11	LE (mm)	0.8	0.2
	Dice	0.68	0.93
	CNR	12.5	17
7	LE (mm)	0.6	0.4
	Dice	0.67	0.91
	CNR	13.5	17.8

Table 2 summarizes the quantitative evaluation of the reconstructions using different forward models. For the target located at three different depths, the proposed model yields higher Dice and CNR with lower LE, indicating that, with the model based on x-ray dosage, CB-XLCT reconstructions have been improved significantly in terms of target shape, localization accuracy, and image contrast, when compared with those reconstructed with the x-ray intensity model.

#### 4.3 Numerical Simulations with Digimouse

The performance of the proposed method was further evaluated with the realistic Digimouse phantom. Tomographic XLCT images reconstructed from simulated projections using different forward models are shown in Fig. 11. It indicates that even for the complicated Digimouse, the proposed model outperforms the intensity-based model in terms of target shape and localization accuracy.

Table 3 summarizes the quantitative evaluation on Digimouse reconstruction using different models. The proposed model yields higher dice and CNR with lower LE, confirming that the dose-based model outperforms the intensity-based model in terms of target shape, localization accuracy, and image contrast.

#### 4.4 Phantom Experiments with Two Targets

To test the performance of the proposed model and method on real imaging system, phantom experiments were performed with two targets positioned at an edge-to-edge distance of 6.3 mm. Tomographic slices of the phantom reconstructed using two different forward models are shown in Fig. 12. The results indicate that for real imaging experiments, the proposed dose-based model still behaves better in shape recovery and location accuracy compared with the conventional intensity-based model.

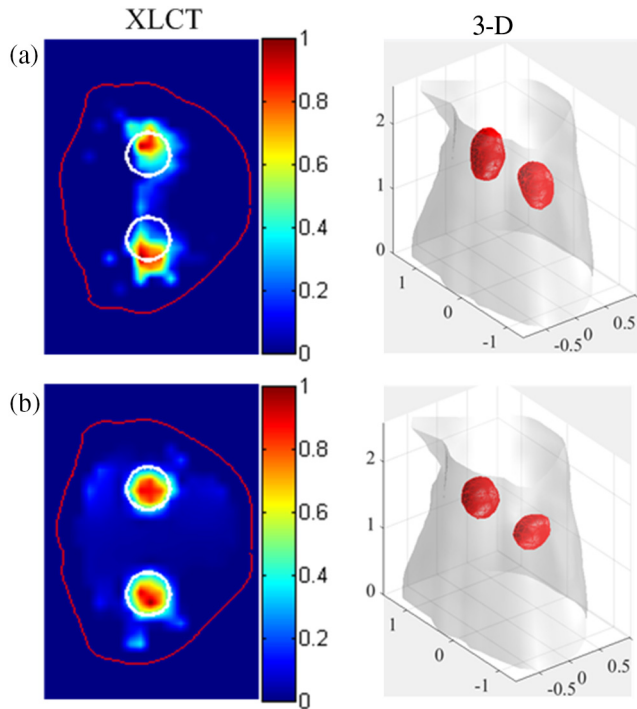


**Fig. 11** CB-XLCT reconstructions of the Digimouse phantom. (a) Reconstructed slice and 3-D rendering using the intensity-based model and (b) reconstructed slice and 3-D rendering using the dose-based model.

**Table 3** Quantitative evaluation on Digimouse reconstructions using different models.

	LE1 (mm)	LE2 (mm)	Dice	CNR
X-ray intensity-based model	0.8	0.9	0.54	7.1
X-ray dosage-based model	0.2	0.3	0.92	8.9

**Table 4** Quantitative analysis of the phantom experiments.

	LE1 (mm)	LE2 (mm)	Dice	CNR
X-ray intensity-based model	0.72	2.4	0.27	1.94
X-ray dosage-based model	0.24	0.4	0.81	4.83

Quantitative evaluation of the phantom reconstructions is given in Table 4. The results indicate that, even in phantom experiments, the proposed model still performs better in target location, shape recovery, and image contrast when compared with the conventional x-ray intensity model.

#### 4.5 Phantom Experiments on Spatial Resolution

To evaluate the performance of the proposed model on improving spatial resolution, phantom experiments were performed by placing two targets with an edge-to-edge distance of 6.3, 2.5, and 1.5 mm, respectively. Figure 13 gives the images reconstructed using different forward models. It indicates that, when the intensity-based model was used, only targets with an edge-to-edge distance of 6.3 mm could be separated. Targets with a distance of 2.5 mm or less could not be distinguished effectively. With the proposed dose-based model, however, even the closest targets with a distance of 1.5 mm could be separated successfully, demonstrating its advantage in improving spatial resolution in real imaging experiments.

### 5 Discussion and Conclusions

In this study, a forward imaging model based on the x-ray absorbed dosage has been proposed for CB-XLCT imaging. Compared with the imaging model used in most XLCT systems, which depends on the intensity distribution of x-rays within the object, the proposed model could better reflect the complicated energy transfer from x-ray photons to luminescence centers of phosphors. CB-XLCT projections calculated with the proposed forward model agree well with actual measurements acquired

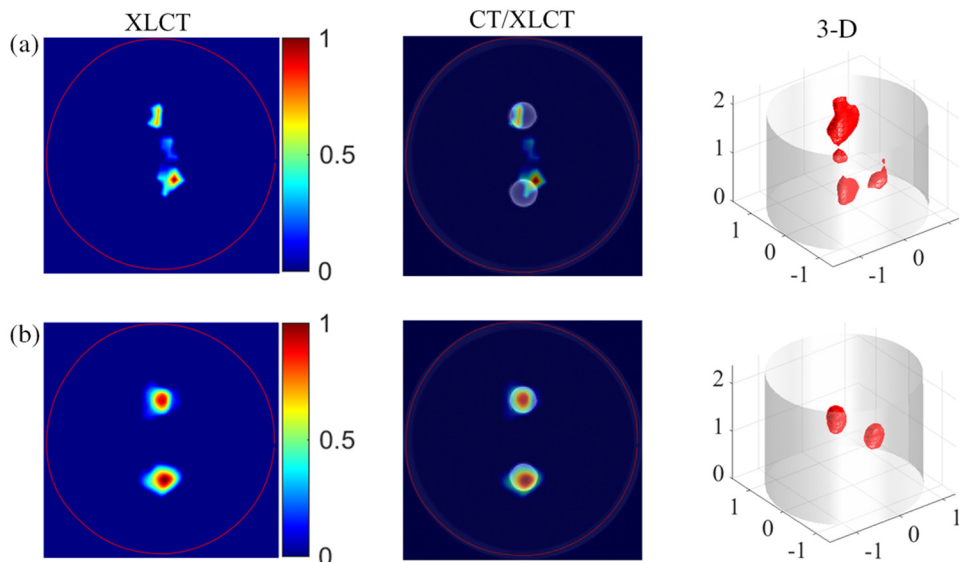


**Fig. 12** Tomographic images of the physical phantom reconstructed using different forward models. (a) Using the intensity-based model and (b) with the proposed dose-based model.

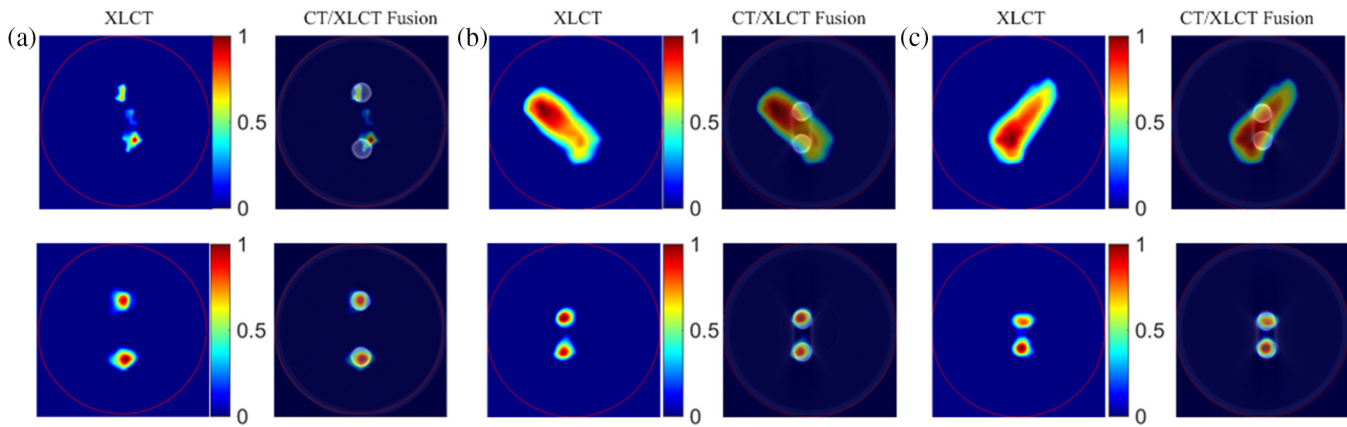


**Fig. 13** Tomographic images of the physical phantom reconstructed using different forward models, with two targets placed at different distances. Upper row: using the intensity-based model, lower row: using the dose-based model. The edge-to-edge distance of two targets is (a) 6.3 mm, (b) 2.5 mm, and (c) 1.5 mm, respectively.

from phantom experiments, indicating that it could model the imaging process of CB-XLCT more accurately.

Numerical simulations with a cylinder phantom and a Digimouse, as well as phantom experiments, confirm the superiority of the proposed model over the intensity-based model. Quantitative evaluation on XLCT reconstructions using LE, DICE, and CNR demonstrates that the proposed model outperforms the intensity-based model in location accuracy, shape recovery, and image contrast of the luminescence targets. In addition, the proposed model behaves quite better in distinguishing closer targets when compared with the conventional x-ray intensity-based model, demonstrating its advantage in improving spatial resolution. All these results clearly demonstrate the power of the proposed dose-based model in improving CB-XLCT reconstructions.

In this study, a density of 7.4 g/ml target in solid state was used mainly because the phosphor ( $\text{Y}_2\text{O}_3:\text{Eu}^{3+}$ ) used is insoluble in water, making it difficult to apply in *in vivo* experiments. In addition, the density of 7.4 g/ml is unrealistic in animal studies. Here, we use it in the phantom experiments to validate the proposed model. Currently, we are working on water-soluble nanophosphors such as  $\text{NaGdF}_4:\text{Eu}^{3+}$ .<sup>36</sup> With improved luminous efficiency, CB-XLCT reconstruction for targets with low concentrations such as 1 mg/ml would be further studied with the proposed model.

Acquiring x-ray dose distribution inside the imaging object is an essential step in the proposed forward model and corresponding reconstruction algorithm. Please note that the estimation of x-ray absorbed dose only involves the energy spectrum of the x-ray source and physical properties of the imaged object related to x-rays, such as scattering and attenuation coefficients. No priors on target position and phosphor concentration are required for x-ray dose estimation. Considering the hybrid imaging capability of XLCT, the attenuation map of the imaged object can be obtained by high-resolution X-CT imaging. Therefore, for future *in-vivo* studies, it is expected that the x-ray dose distribution for the excitation process could be estimated accurately by Monte Carlo simulation packages, such as GATE, based on the simulation of experimental conditions such as x-ray source configuration and the attenuation map of the imaging object, which could be acquired by simultaneous X-CT imaging.

In this study, the dose distribution was estimated by the widely used GATE package performed on a computer with

a 40-core processor of 2.5 GHz and 64 GB RAM. For each projection with a total number of x-ray photons of  $10^8$ , the calculation time was 50 min. With multithread parallel computing, the dose distributions of eight angles could be calculated simultaneously. Therefore, the total computational cost was 150 min for dose estimation of 24 angles acquired in a XLCT scan, while the computing time for x-ray intensity distribution was 95 s under the same measurement condition. However, the computation loads for x-ray intensity distribution and dose estimation would only affect the constructing time of  $W$  in the forward model, not the imaging and reconstruction time. In this study, all XLCT images were reconstructed using the ADAPTIVK algorithm. With the same reconstruction parameters, such as stopping criterion and iteration number, the reconstruction time mainly depended on the size of  $W$  and  $\Phi_{\text{meas}}$ . For example, the reconstruction time with the proposed method was 155 s, while the reconstruction time with the traditional forward model was 160 s for the phantom experiments with two targets, when the stopping criterion  $\alpha_{\text{stop}}$  was set as  $10^{-8}$  and the number of iterations was set as 8. In addition to GATE, there are other MC packages that could be used for x-ray dose estimation, such as Geant4, Electron-Gamma-Shower, PENELOPE, etc.<sup>14,37</sup> The computational load could be further reduced by selecting an efficient MC package and the use of graphic processing unit acceleration technology.

In this study, based on the proposed dose-based forward model, the adaptive Tikhonov regularization method was adopted for adaptive reconstruction of CB-XLCT imaging. To further improve the image quality, statistical reconstruction methods using regularizations, such as the Bayesian method based on Gaussian Markov random field proposed by Zhang et al.,<sup>22</sup> total variance (TV) regularization,<sup>38</sup> and Laplace regularization,<sup>39</sup> can be used or extended for CB-XLCT imaging. The combination of the proposed model with regularized reconstruction is under investigation.

In summary, we established a forward model based on x-ray absorbed dosage for CB-XLCT imaging. The reconstruction result of numerical simulations and phantom experiments indicates that, compared with the traditional model based on x-ray intensity, the proposed model can improve the quality of CB-XLCT imaging significantly. There are several issues worth further study. First, in this study, the phantom was scanned twice to collect the x-ray transmission and luminescence data

separately. The imaging time could be further reduced and anatomical variations between two scans could be alleviated if two sets of data can be collected simultaneously. Second, the CB-XLCT reconstruction for the target with low concentrations such as 1 and 0.1 mg/ml based on the proposed model could be further studied. Finally, the feasibility of the proposed model has been evaluated only with phantom experiments. In future studies, *in vivo* experiments will be performed for further validation with the development of water-soluble nanophosphors.

### Disclosures

The authors declare that there are no conflicts of interest related to this article.

### References

- G. Prax et al., "X-ray luminescence computed tomography via selective excitation: a feasibility study," *IEEE Trans. Med. Imaging* **29**(12), 1992–1999 (2010).
- G. Prax et al., "Tomographic molecular imaging of x-ray-excitable nanoparticles," *Opt. Lett.* **35**(20), 3345–3347 (2010).
- C. M. Carpenter et al., "Hybrid x-ray/optical luminescence imaging: characterization of experimental conditions," *Med. Phys.* **37**(8), 4011–4018 (2010).
- G. Wang et al., "In vivo mouse studies with bioluminescence tomography," *Opt. Express* **14**(17), 7801–7809 (2006).
- J. Feng et al., "Bioluminescence tomography imaging in vivo: recent advances," *IEEE J. Sel. Top. Quantum Electron.* **18**(4), 1394–1402 (2012).
- A. Ale et al., "FMT-XCT: in vivo animal studies with hybrid fluorescence molecular tomography-x-ray computed tomography," *Nat. Methods* **9**, 615–620 (2012).
- G. Zhang et al., "Imaging of pharmacokinetic rates of indocyanine green in mouse liver with a hybrid fluorescence molecular tomography/x-ray computed tomography system," *J. Biomed. Opt.* **18**(4), 040505 (2013).
- C. Sun et al., "Synthesis and radioluminescence of PEGylated Eu<sup>3+</sup>-doped nanophosphors as bioimaging probes," *Adv. Mater.* **23**(24), H195–H199 (2011).
- S. Ahn, S. Y. Jung, and S. J. Lee, "Gold nanoparticle contrast agents in advanced x-ray imaging technologies," *Molecules* **18**(5), 5858–5890 (2013).
- H. Chen, M. M. Rogalski, and J. N. Anker, "Advances in functional x-ray imaging techniques and contrast agents," *Phys. Chem. Chem. Phys.* **14**(39), 13469–13486 (2012).
- Y. Osakada et al., "X-ray excitable luminescent polymer dots doped with an iridium(III) complex," *Chem. Commun.* **49**(39), 4319–4321 (2013).
- J. Shen, L. Zhao, and G. Han, "Lanthanide-doped upconverting luminescent nanoparticle platforms for optical imaging-guided drug delivery and therapy," *Adv. Drug Delivery Rev.* **65**(5), 744–755 (2013).
- L. Sudheendra et al., "NaGdF<sub>4</sub>:Eu<sup>3+</sup> nanoparticles for enhanced x-ray excited optical imaging," *Chem. Mater.* **26**(5), 1881–1888 (2014).
- C. Li et al., "X-ray luminescence optical tomography imaging: experimental studies," *Opt. Lett.* **38**(13), 2339–2341 (2013).
- C. Li, A. Martínezdávalos, and S. R. Cherry, "Numerical simulation of x-ray luminescence optical tomography for small-animal imaging," *J. Biomed. Opt.* **19**(4), 046002 (2014).
- W. Cong, H. Shen, and G. Wang, "Spectrally resolving and scattering-compensated x-ray luminescence/fluorescence computed tomography," *J. Biomed. Opt.* **16**(6), 066014 (2011).
- D. Chen et al., "Cone beam x-ray luminescence computed tomography: a feasibility study," *Med. Phys.* **40**(3), 031111 (2013).
- D. Chen et al., "Quantitative cone beam x-ray luminescence tomography/x-ray computed tomography imaging," *Appl. Phys. Lett.* **105**(19), 191104 (2014).
- D. Chen et al., "X-ray luminescence computed tomography imaging based on x-ray distribution model and adaptively split Bregman method," *Biomed. Opt. Express* **6**(7), 2649–2663 (2015).
- X. Liu, Q. Liao, and H. Wang, "In vivo x-ray luminescence tomographic imaging with single-view data," *Opt. Lett.* **38**(22), 4530–4533 (2013).
- X. Liu, Q. Liao, and H. Wang, "Fast x-ray luminescence computed tomography imaging," *IEEE Trans. Biomed. Eng.* **61**(6), 1621–1627 (2014).
- G. Zhang et al., "Cone beam x-ray luminescence computed tomography based on Bayesian method," *IEEE Trans. Med. Imaging* **36**(1), 225–235 (2017).
- W. M. Yen and M. J. Weber, *Inorganic Phosphors: Compositions, Preparation and Optical Properties*, CRC Press, Boca Raton (2004).
- P. Lecoq et al., *Inorganic Scintillators for Detector Systems*, Springer, Berlin, Heidelberg (2006).
- A. M. Pires, M. R. Davolos, and E. B. Stucchi, "Eu<sup>3+</sup> as a spectroscopic probe in phosphors based on spherical fine particle gadolinium compounds," *Int. J. Inorg. Mater.* **3**(7), 785–790 (2001).
- S. Jan et al., "GATE V6: a major enhancement of the GATE simulation platform enabling modelling of CT and radiotherapy," *Phys. Med. Biol.* **56**(4), 881–901 (2011).
- D. Sarrut et al., "A review of the use and potential of the GATE Monte Carlo simulation code for radiation therapy and dosimetry applications," *Med. Phys.* **41**(6), 064301 (2014).
- M. Schweiger et al., "The finite element method for the propagation of light in scattering media: boundary and source conditions," *Med. Phys.* **22**(11), 1779–1792 (1995).
- Y. Lv et al., "A multilevel adaptive finite element algorithm for bioluminescence tomography," *Opt. Express* **14**(18), 8211–8223 (2006).
- X. Cao et al., "An adaptive Tikhonov regularization method for fluorescence molecular tomography," *Med. Biol. Eng. Comput.* **51**(8), 849–858 (2013).
- W. Zhang et al., "Multiple pinhole collimator based x-ray luminescence computed tomography," *Biomed. Opt. Express* **7**(7), 2506–2523 (2016).
- D. Dong et al., "Automated recovery of the center of rotation in optical projection tomography in the presence of scattering," *IEEE J. Biomed. Health Inf.* **17**(1), 198–204 (2013).
- S. Zhu et al., "Cone beam micro-CT system for small animal imaging and performance evaluation," *Int. J. Biomed. Imaging* **2009**, 1–9 (2009).
- J. M. Boone et al., "Simulation of X-ray spectra," <https://www.oem-xray-components.siemens.com/x-ray-spectra-simulation> (2017).
- Y. An et al., "A novel region reconstruction method for fluorescence molecular tomography," *IEEE Trans. Biomed. Eng.* **62**(7), 1818–1826 (2015).
- W. Zhang et al., "Sub-10 nm water-dispersible β-NaGdF<sub>4</sub>:X% Eu<sup>3+</sup> nanoparticles with enhanced biocompatibility for in vivo x-ray luminescence computed tomography," *ACS Appl. Mater. Interfaces* **9**(46), 39985–39993 (2017).
- A. Mittone et al., "An efficient numerical tool for dose deposition prediction applied to synchrotron medical imaging and radiation therapy," *J. Synchrotron Radiat.* **20**(5), 785–792 (2013).
- J. Rong et al., "CT reconstruction from few-views with anisotropic edge-guided total variance," *Nucl. Instrum. Methods* **820**, 54–64 (2016).
- Y. Gao et al., "Bioluminescence tomography based on Gaussian weighted Laplace prior regularization for in vivo morphological imaging of glioma," *IEEE Trans. Med. Imaging* **36**(11), 2343–2354 (2017).

**Tianshuai Liu** is a PhD candidate in the Department of Biomedical Engineering at Fourth Military Medical University of China. His current research interests are in the field of x-ray imaging model and image reconstruction techniques.

**Junyan Rong** received her PhD in physics from the Institute of High Energy Physics, Chinese Academy of Sciences, Beijing, China, in 2009. Currently, she is an assistant professor in the Department of Biomedical Engineering at Fourth Military Medical University of China. Her research interests include CT technique and multimodality biomedical imaging.

**Hongbing Lu** is a professor in the Department of Biomedical Engineering at Fourth Military Medical University of China. She received her PhD in biomedical engineering from Tsinghua University of China, in 1998, followed by postdoctoral training in radiology at the State University of New York at Stony Brook, until 2002. Her research interests cover a spectrum from medical image reconstruction to image analysis for computer-aided detection (CADe) and diagnosis (CADx).

Biographies for the other authors are not available.